CHAPTER FIVE

Dynamics of Heterogeneity in Fluid Membranes

Shigeyuki Komura*[1], Sanoop Ramachandran[†], Kazuhiko Seki[‡], Masayuki Imai[§]

*Department of Chemistry, Graduate School of Science and Engineering, Tokyo Metropolitan University, Tokyo, Japan
[†]Physique des Polymères, Université Libre de Bruxelles, Brussels, Belgium
[‡]National Institute of Advanced Industrial Science and Technology (AIST), Tsukuba, Japan
[§]Department of Physics, Faculty of Science, Tohoku University, Sendai, Japan
[1]Corresponding author: e-mail address: komura@tmu.ac.jp

Contents

Abstract

In this chapter, we investigate the dynamics of heterogeneity observed in multicomponent fluid membranes, particularly focusing on hydrodynamic effects due to the membrane and solvent. Two situations are discussed separately: above and below the miscibility transition temperature. In the former case, we calculate the wave number dependence of the effective diffusion coefficient by changing the temperature and/or the thickness of the bulk fluid. We also obtain the effective diffusion coefficient when multicomponent membranes are regarded as two-dimensional microemulsions. For the case below the transition temperature, we study the domain growth exponent in a binary membrane using a particle-based simulation method. With the addition

Advances in Planar Lipid Bilayers and Liposomes, Volume 16
ISSN 1554-4516
http://dx.doi.org/10.1016/B978-0-12-396534-9.00005-2

of bulk solvent, a change in the growth exponent from two- to three-dimensional nature is observed. Along with the measurement of correlated diffusion, we conclude that the phase separation takes place through the Brownian coagulation process in our simulation. We shall review some other works which are related to the present subject.

1. INTRODUCTION

Biological membranes typically contain various components such as lipid mixtures, sterols, and proteins that are indispensable to cell functions [1,2]. Rather than being uniformly distributed in the membrane, there is growing evidence that some cellular components are incorporated in domains arising from lateral lipid segregation in membranes. In 1997, Simons and Ikonen proposed a hypothesis which suggested that some lipids organize themselves into submicron-sized domains termed "lipid rafts" [3]. It was postulated that lipid rafts serve as platforms for proteins which attribute certain functionality to each domain.

In 2006, the definition of lipid rafts was proposed as follows [4]: "Membrane rafts are small (10–200 nm), heterogeneous, highly dynamic, sterol- and sphingolipid-enriched domains that compartmentalize cellular processes. Small rafts can sometimes be stabilized to form larger platforms through protein-protein and protein-lipid interactions." In spite of such a definition, the existence of lipid rafts is still debatable [5]. This is because lipid rafts have not yet been directly observed *in vivo*. One of the key issues that has been repeatedly asked is concerned with the lateral size and lifetime of lipid domains or clusters. The reported value ranges from 20 to 200 nm for the size, and from 10^{-2} to 10^{3} s for the lifetime [6]. Recently, a high-resolution observation of the lipid dynamics in living cells is achieved using stimulated emission depletion fluorescent microscopy [7]. They reported that sphingomyeline and membrane proteins are transiently (10–20 ms) trapped in about 20 nm diameter areas.

Stimulated by the lipid raft hypothesis, studies on artificial model membranes have been developed intensively in the last decade. Especially, the phase behavior of ternary giant vesicles composed of saturated lipids with high chain-melting temperature, unsaturated lipids with low chain-melting temperature, and cholesterol has been investigated for various mixtures [8,9]. It is known that such a ternary membrane is homogeneously mixed in the high-temperature region. By decreasing the temperature, the membrane undergoes a phase separation between the coexisting liquid-ordered (L_o) and liquid-disordered (L_d) phases. As a typical example, we show in Fig. 5.1 the phase diagram of a ternary vesicle consisting of DOPC (dioleoylphosphatidylcholine), PSM

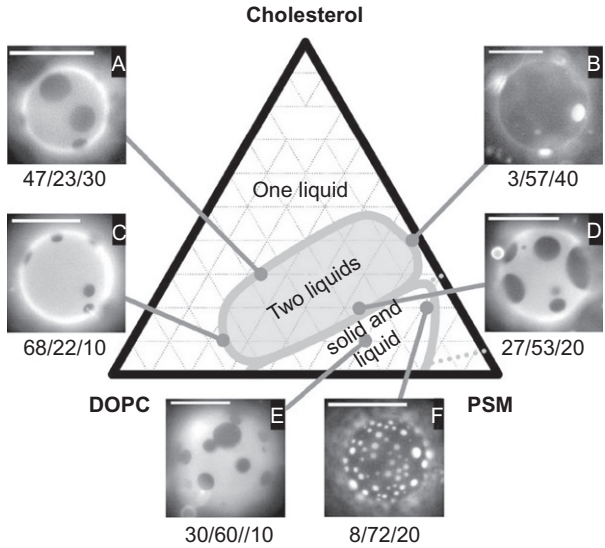

Figure 5.1 Phases observed by fluorescence microscopy of giant unilamellar vesicles containing mixture of DOPC, PSM, and cholesterol at 298 K. The dark liquid phase is rich in PSM and cholesterol, while the bright liquid phase is rich in DOPC. *Adapted from Ref. [10].*

(*N*-palmitoyl-D-sphingomyelin) and cholesterol together with several fluorescence micrographs [10]. In these pictures, dark liquid domains are rich in PSM and cholesterol, while bright liquid ones are rich in DOPC. The minority liquid phase forms circular domains which undergo lateral Brownian motion on the vesicle. In order to determine the ternary phase diagrams and to identify the domain morphologies, a large amount of research has been conducted using various experimental techniques [11].

On the other hand, behaviors of multicomponent membranes above the transition temperature have also gained much attention. Performing deuterium NMR experiments, Veatch *et al.* made a notable attempt to investigate critical fluctuations in lipid mixtures consisting of DOPC, DPPC (dipalmitoylphosphatidylcholine), and cholesterol [12]. A broadening of NMR resonances in the vicinity of the critical point was attributed to the compositional fluctuations on the scale less than 50 nm in the membrane. A more quantitative analysis of critical fluctuations using fluorescence microscopy was addressed by Honerkamp-Smith *et al.* for ternary mixtures of DPPC, diPhyPC (diphytanoylphosphatidylcholine), and cholesterol [13]. Typical microscope pictures of concentration fluctuations are shown in Fig. 5.2 for higher temperatures. From the measurement of the critical exponents, the authors concluded that the critical behavior in ternary membranes belongs to the universality class

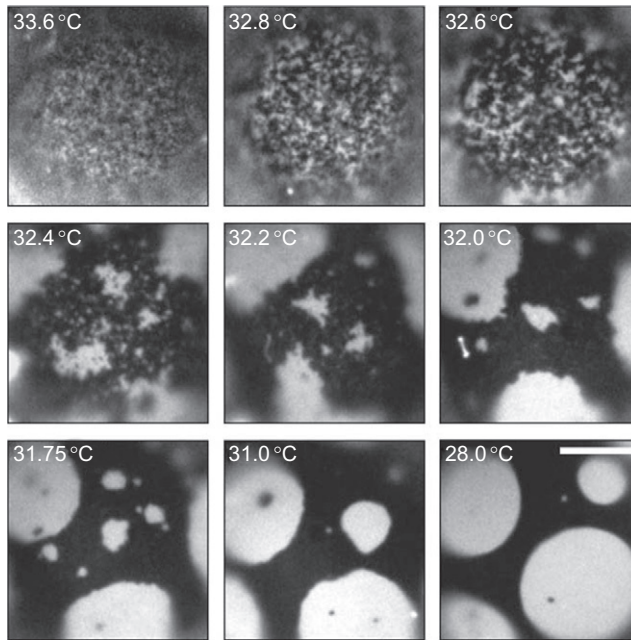

Figure 5.2 Giant vesicle consisting of DPPC, diPhyPC, and cholesterol passing through a critical temperature at $T_c \approx 32.5\,^{\circ}\mathrm{C}$. For temperatures above T_c, the vesicle exhibits concentration fluctuations. For temperatures below T_c, the vesicle undergoes a macroscopic phase separation. The scale bar corresponds to 20 μm. *Adapted from Ref. [13].*

of the two-dimensional (2D) Ising model [14]. Furthermore, by analyzing the correlation length and the line tension, it was shown that giant plasma membrane vesicles extracted from that of living rat basophil leukemia cells also exhibit a critical behavior [15]. These results allow us to speculate that lateral heterogeneity present in real cell membranes at physiological conditions could correspond to critical fluctuations.

As mentioned in the first paragraph, it is important to note that lipid rafts are highly dynamical objects. Being stimulated by various experiments, we shall discuss in this chapter the dynamics of heterogeneity in multicomponent membranes. It will be stressed that the hydrodynamic interaction mediated not only by the fluid membrane itself but also by the bulk solvent plays an essential role in the dynamics of multicomponent membranes at large scales. We discuss the cases of above and below the miscibility transition temperature separately.

In Section 2, we first provide a general framework of the membrane hydrodynamics. In Section 3, we investigate the dynamics of critical concentration fluctuations above the transition temperature. Based on the Ginzburg–Landau approach with full hydrodynamics, we calculate the wave

number dependence of the effective diffusion coefficient. We shall also consider the situation when the multicomponent membranes form microemulsions [16]. In Section 4, we study the domain growth dynamics below the transition temperature using dissipative particle dynamics (DPD) simulations. We show that the presence of a bulk fluid will alter the domain growth exponent from that of 2D to 3D, indicating a significant role played by the membrane–solvent coupling. In order to elucidate the underlying physical mechanism of this effect, we look into the diffusion properties in the membrane by measuring two-particle correlated diffusion. We show that quasi-2D phase separation proceeds by the Brownian coagulation (BC) mechanism which reflects the 3D nature of the bulk solvent. We will also compare our results with the related works in the literatures.

2. MEMBRANE HYDRODYNAMICS

In this section, we first establish the governing equations for the fluid membrane and its surrounding environment. Our aim is to derive the membrane mobility tensors which will be used in the later sections. More details of the calculation are given in Refs. [17,18].

As shown in Fig. 5.3, we assume that the membrane is an infinite planar sheet of liquid, and its out-of-plane fluctuations are totally neglected, which is justified for typical bending rigidities of bilayers. The liquid membrane is embedded in a bulk fluid such as water or solvent that is bounded by hard walls. Such a situation is worth considering because biological membranes interact strongly with other cells, substrates, or even the underlying cytoskeleton which can affect the structural and transport properties of the

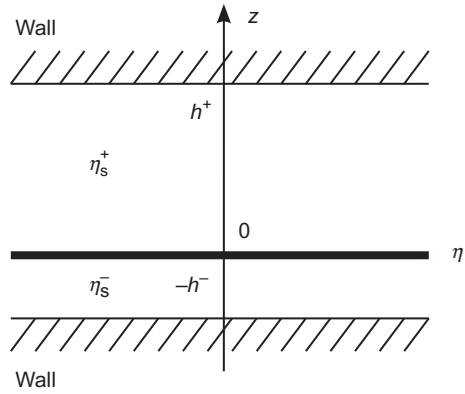

Figure 5.3 Schematic picture showing a planar liquid membrane having 2D viscosity η located at $z=0$. It is sandwiched by a solvent of 3D viscosity $\eta_s^{\pm}$. Two impenetrable walls are located at $z=\pm h^{\pm}$ bounding the solvent.

membrane. Let $\mathbf{v}(\mathbf{r})$ be the 2D velocity of the membrane fluid and the 2D vector $\mathbf{r}=(x,y)$ represents a point in the plane of the membrane. We first assume the membrane to be incompressible

$$\nabla\cdot\mathbf{v}=0, \tag{5.1}$$

where ∇ is a 2D differential operator. We work in the low-Reynolds number regime of the membrane hydrodynamics so that the inertial effects can be neglected. This allows us to use the 2D Stokes equation given by [19]

$$\eta\nabla^2\mathbf{v}-\nabla p+\mathbf{f}_\mathrm{s}+\mathbf{F}=0, \tag{5.2}$$

where η is the 2D membrane viscosity, $p(\mathbf{r})$ the 2D in-plane pressure, $\mathbf{f}_\mathrm{s}(\mathbf{r})$ the force exerted on the membrane by the surrounding fluid ("s" stands for the solvent), and $\mathbf{F}(\mathbf{r})$ is any other force acting on the membrane which we shall discuss in later sections.

As presented in Fig. 5.3, the membrane is fixed in the xy-plane at $z=0$. The upper ($z>0$) and the lower ($z<0$) fluid regions are denoted by "+" and "−," respectively. The velocities and pressures in these regions are written as $\mathbf{v}^\pm(\mathbf{r},z)$ and $p^\pm(\mathbf{r},z)$, respectively. Since the 3D viscosity of the upper and the lower solvent can be different, we denote them as $\eta_\mathrm{s}^\pm$, respectively. Consider the situation in which impenetrable walls are located at $z=\pm h^\pm$, where h^+ and h^- can be different in general. Similar to the liquid membrane, the solvent in both regions are taken to be incompressible

$$\tilde{\nabla}\cdot\mathbf{v}^\pm=0, \tag{5.3}$$

where $\tilde{\nabla}$ represents a 3D differential operator. We also neglect the solvent inertia, and hence, it obeys the 3D Stokes equations

$$\eta_\mathrm{s}^\pm\tilde{\nabla}^2\mathbf{v}^\pm-\tilde{\nabla}p^\pm=0. \tag{5.4}$$

The presence of the surrounding solvent is important because it exerts force on the fluid membrane. This force, indicated as $\mathbf{f}_\mathrm{s}$ in Eq. (5.2), is given by the projection of $(\boldsymbol{\sigma}^+-\boldsymbol{\sigma}^-)_{z=0}\cdot\hat{\mathbf{e}}_z$ on the xy-plane. Here $\hat{\mathbf{e}}_z$ is the unit vector along the z-axis, and $\boldsymbol{\sigma}^\pm$ are the stress tensors due to the solvent

$$\boldsymbol{\sigma}^\pm=-p^\pm\mathbf{I}+\eta_\mathrm{s}^\pm\left[\tilde{\nabla}\mathbf{v}^\pm+\left(\tilde{\nabla}\mathbf{v}^\pm\right)^\mathrm{T}\right]. \tag{5.5}$$

In the above, $\mathbf{I}$ is the identity tensor and the superscript "T" indicates the transpose.

Using the stick boundary conditions at $z=0$ and $z=\pm h^\pm$, we solve the hydrodynamic equations (5.3) and (5.4) to obtain $\mathbf{f}_\mathrm{s}$. Then we calculate the membrane velocity from Eq. (5.2) as

$$\mathbf{v}[\mathbf{k}] = \mathbf{G}[\mathbf{k}]\cdot\mathbf{F}[\mathbf{k}], \tag{5.6}$$

where $\mathbf{v}[\mathbf{k}]$ and others are the Fourier components defined such as by

$$\mathbf{v}(\mathbf{r}) = \int \frac{d\mathbf{k}}{(2\pi)^2}\mathbf{v}[\mathbf{k}]\exp(i\mathbf{k}\cdot\mathbf{r}), \tag{5.7}$$

with $\mathbf{k} = (k_x, k_y)$. After some calculations, one can show that the mobility tensor $\mathbf{G}[\mathbf{k}]$ in Fourier space is given by [17,18]

$$G_{\alpha\beta}[\mathbf{k}] = \frac{1}{\eta k^2 + k\left[\eta_s^+ \coth(kh^+) + \eta_s^- \coth(kh^-)\right]}\left(\delta_{\alpha\beta} - \frac{k_\alpha k_\beta}{k^2}\right), \tag{5.8}$$

with $\alpha, \beta = x, y$ and $k = |\mathbf{k}|$. For simplicity, we consider the case when the two walls are located at equal distances from the membrane, that is, $h^+ = h^- = h$. Then the above mobility tensor becomes

$$G_{\alpha\beta}[\mathbf{k}] = \frac{1}{\eta[k^2 + \nu k\coth(kh)]}\left(\delta_{\alpha\beta} - \frac{k_\alpha k_\beta}{k^2}\right), \tag{5.9}$$

where $\nu^{-1} = \eta/2\eta_s$ with $\eta_s = (\eta_s^+ + \eta_s^-)/2$. An almost equivalent expression to Eq. (5.9) has been derived for Langmuir monolayers in which there is only one wall or a substrate [20,21]. In the following, we will employ Eq. (5.9) as the general membrane mobility tensor.

We now discuss the two limiting situations of Eq. (5.9). Saffman and Delbrück (SD) investigated the case when the two walls are located infinitely away from the membrane, which is called as the free membrane case [22–24]. Taking the limit of $kh \gg 1$ in Eq. (5.9), the mobility tensor becomes [25,26]

$$G_{\alpha\beta}^{\text{free}}[\mathbf{k}] = \frac{1}{\eta(k^2 + \nu k)}\left(\delta_{\alpha\beta} - \frac{k_\alpha k_\beta}{k^2}\right). \tag{5.10}$$

The quantity ν^{-1} is called as the SD hydrodynamic screening length. The real space expression of this mobility tensor is obtained by the Fourier transform of Eq. (5.10) [21,25,26]

$$\begin{aligned} G_{\alpha\beta}^{\text{free}}(\mathbf{r}) = {} & \frac{1}{4\eta}\left[\mathbf{H}_0(\nu r) - Y_0(\nu r) + \frac{2}{\pi\nu^2 r^2} - \frac{\mathbf{H}_1(\nu r)}{\nu r} + \frac{Y_1(\nu r)}{\nu r}\right]\delta_{\alpha\beta} \\ & + \frac{1}{4\eta}\left[-\frac{4}{\pi\nu^2 r^2} + \frac{2\mathbf{H}_1(\nu r)}{\nu r} - \frac{2Y_1(\nu r)}{\nu r} - \mathbf{H}_0(\nu r) + Y_0(\nu r)\right]\frac{r_\alpha r_\beta}{r^2}, \end{aligned} \tag{5.11}$$

where $r = |\mathbf{r}|$. In the above, $\mathbf{H}_n(z)$ are Struve functions and $Y_n(z)$ are Bessel functions of the second kind.

Evans and Sackmann (ES) considered the opposite $kh \ll 1$ limit, for which the membrane is confined between the two walls although the solvent is still left [27]. In this case, Eq. (5.9) takes the following form:

$$G^{\mathrm{con}}_{\alpha\beta}[\mathbf{k}] = \frac{1}{\eta(k^2+\kappa^2)}\left(\delta_{\alpha\beta} - \frac{k_\alpha k_\beta}{k^2}\right). \tag{5.12}$$

In the above, $\kappa^{-1} = \sqrt{\nu^{-1}h}$ is called as the ES hydrodynamic screening length, and it is the geometric mean of ν^{-1} and h [28]. The above mobility tensor was used in a phenomenological membrane hydrodynamic model with momentum decay [26,29–31]. The real space representation of the above mobility tensor becomes

$$\begin{aligned} G^{\mathrm{con}}_{\alpha\beta}(\mathbf{r}) = {} & \frac{1}{2\pi\eta}\left[K_0(\kappa r) + \frac{K_1(\kappa r)}{\kappa r} - \frac{1}{\kappa^2 r^2}\right]\delta_{\alpha\beta} \\ & + \frac{1}{2\pi\eta}\left[-K_0(\kappa r) - \frac{2K_1(\kappa r)}{\kappa r} + \frac{2}{\kappa^2 r^2}\right]\frac{r_\alpha r_\beta}{r^2}, \end{aligned} \tag{5.13}$$

where $K_n(z)$ are the modified Bessel functions of the second kind. In Section 3, we shall mainly use the general mobility tensor Eq. (5.9), whereas either Eq. (5.10) or (5.12) is used in Section 4.

3. DYNAMICS OF CONCENTRATION FLUCTUATIONS

3.1. Time-dependent Ginzburg–Landau model

In this section, we use the idea of critical dynamics to calculate the effective diffusion coefficient in multicomponent lipid membranes. Based on Ginzburg–Landau approach with full hydrodynamics, we calculate the decay rate of the concentration fluctuations occurring in membranes [32,33]. We deal with the general case where the membrane is surrounded by a bulk solvent and two walls as depicted in Fig. 5.3. We also study the situation when the multicomponent membranes form 2D microemulsions [16]. This interesting viewpoint is motivated by a recent work which predicts the reduction of the line tension in membranes containing saturated, unsaturated, and hybrid lipids (one tail saturated and the other unsaturated) [34–37]. We shall explore the concentration fluctuations in 2D microemulsion with full hydrodynamics.

Consider a two-component fluid membrane composed of lipid A and lipid B whose local area fractions are denoted by $\phi_{\mathrm{A}}(\mathbf{r})$ and $\phi_{\mathrm{B}}(\mathbf{r})$, respectively. Since the relation $\phi_{\mathrm{A}}(\mathbf{r}) + \phi_{\mathrm{B}}(\mathbf{r}) = 1$ holds, we introduce a new

variable defined by $\psi(\mathbf{r}) = \phi_A(\mathbf{r}) - \phi_B(\mathbf{r})$. Then the simplest form of the free-energy functional $\mathcal{F}\{\psi\}$ describing the fluctuation around the homogeneous state is

$$\mathcal{F}\{\psi\} = \int d\mathbf{r}\left[\frac{a}{2}\psi^2 + \frac{c}{2}(\nabla\psi)^2\right], \tag{5.14}$$

where $a > 0$ is proportional to the temperature difference from the critical temperature T_c and $c > 0$ is related to the line tension.

The time evolution of concentration in the presence of hydrodynamic flow is given by the time-dependent Ginzburg–Landau equation for a conserved order parameter [38]

$$\frac{\partial\psi}{\partial t} + \nabla\cdot(\mathbf{v}\psi) = \Lambda\nabla^2\frac{\delta F}{\delta\psi}, \tag{5.15}$$

where Λ is the kinetic coefficient. In the membrane hydrodynamic equation (5.2), we need to incorporate the thermodynamic force due to the concentration fluctuations. Hence we have

$$\mathbf{F} = -\psi\nabla\frac{\delta\mathcal{F}}{\delta\psi}. \tag{5.16}$$

We implicitly assume that the relaxation of the velocity $\mathbf{v}$ is much faster than that of concentration ψ. The membrane velocity can be formally solved as follows using the appropriate 2D mobility tensor $G_{\alpha\beta}(\mathbf{r},\mathbf{r}')$ derived in the previous section

$$v_\alpha(\mathbf{r},t) = \int d\mathbf{r}' G_{\alpha\beta}(\mathbf{r},\mathbf{r}')\left(\nabla'_\beta\psi\right)\frac{\delta\mathcal{F}}{\delta\psi(\mathbf{r}')}. \tag{5.17}$$

Since our interest is in the concentration fluctuations around the homogeneous state, we define $\delta\psi(\mathbf{r},t) = \psi(\mathbf{r},t) - \bar{\psi}$, where the bar indicates the spatial average. The free-energy functional expanded in powers of $\delta\psi$ becomes

$$\mathcal{F}\{\delta\psi\} = \int d\mathbf{r}\left[\frac{a}{2}(\delta\psi)^2 + \frac{c}{2}(\nabla\delta\psi)^2\right]. \tag{5.18}$$

Substituting Eq. (5.17) into Eq. (5.15), we get

$$\frac{\partial\delta\psi(\mathbf{r},t)}{\partial t} = \Lambda\nabla^2\frac{\delta\mathcal{F}}{\delta(\delta\psi)} - \int d\mathbf{r}'(\nabla_\alpha\delta\psi(\mathbf{r}))G_{\alpha\beta}(\mathbf{r},\mathbf{r}')\left(\nabla'_\beta\delta\psi(\mathbf{r}')\right)\frac{\delta\mathcal{F}}{\delta(\delta\psi(\mathbf{r}'))}. \tag{5.19}$$

We now consider the dynamics of the time-correlation function defined by

$$S(\mathbf{r},t)=\langle\delta\psi(\mathbf{r}_1,t)\delta\psi(\mathbf{r}_2,0)\rangle, \tag{5.20}$$

where $\mathbf{r}=\mathbf{r}_2-\mathbf{r}_1$. Within the factorization approximation [39], the spatial Fourier transform of $S(\mathbf{r},t)$ defined by

$$S[\mathbf{k},t]=\int d\mathbf{r}S(\mathbf{r},t)\exp(-i\mathbf{k}\cdot\mathbf{r}) \tag{5.21}$$

satisfies the following equation

$$\frac{\partial S[\mathbf{k},t]}{\partial t}=-\left(\Gamma^{(1)}[\mathbf{k}]+\Gamma^{(2)}[\mathbf{k}]\right)S[\mathbf{k},t]. \tag{5.22}$$

The first term, $\Gamma^{(1)}[\mathbf{k}]$, denotes the van Hove part of the relaxation rate given by

$$\Gamma^{(1)}[\mathbf{k}]=\Lambda k_{\mathrm{B}}Tk^2\chi^{-1}[\mathbf{k}]. \tag{5.23}$$

Here, the static correlation function is defined by

$$\chi[\mathbf{k}]=\langle\delta\psi[\mathbf{k}]\delta\psi[-\mathbf{k}]\rangle=\frac{k_{\mathrm{B}}T}{c\left(k^2+\xi^{-2}\right)}, \tag{5.24}$$

where $\xi=(c/a)^{1/2}$ is the correlation length, k_{B} the Boltzmann constant, and T the temperature.

As for the second term in Eq. (5.22), $\Gamma^{(2)}[\mathbf{k}]$ denotes the hydrodynamic part of the decay rate given by

$$\Gamma^{(2)}[\mathbf{k}]=\frac{1}{\chi[\mathbf{k}]}\int\frac{d\mathbf{q}}{(2\pi)^2}k_\alpha G_{\alpha\beta}[\mathbf{q}]k_\beta\chi[\mathbf{k}+\mathbf{q}]. \tag{5.25}$$

When we use Eq. (5.9) for the mobility tensor $G_{\alpha\beta}$, the hydrodynamic part of the decay rate is expressed with an integral as

$$\Gamma^{(2)}[\mathbf{k}]=\frac{k_{\mathrm{B}}T}{\eta\chi[\mathbf{k}]}\int\frac{d\mathbf{q}}{(2\pi)^2}\frac{\chi[\mathbf{q}]}{|\mathbf{k}-\mathbf{q}|^2+\nu|\mathbf{k}-\mathbf{q}|\coth(|\mathbf{k}-\mathbf{q}|h)}\frac{k^2q^2-(\mathbf{k}\cdot\mathbf{q})^2}{|\mathbf{k}-\mathbf{q}|^2}. \tag{5.26}$$

3.2. Effective diffusion coefficient

We now introduce an effective diffusion coefficient (due only to the hydrodynamic part) $D[\mathbf{k}]$ defined by

$$\Gamma^{(2)}[\mathbf{k}] = k^2 D[\mathbf{k}]. \tag{5.27}$$

In order to deal with dimensionless quantities, we rescale all the lengths by the SD hydrodynamic screening length $\nu^{-1} = \eta/2\eta_s$ such that $K = k/\nu$, $Q = q/\nu$, $X = \xi\nu$, and $H = h\nu$. Then $D[\mathbf{k}]$ can be rewritten as

$$D[K;X,H] = \frac{k_B T}{4\pi^2\eta}\left(1+K^2X^2\right)\int_0^\infty \mathrm{d}Q \int_0^{2\pi} \mathrm{d}\theta \frac{Q^3 \sin^2\theta}{\left(1+Q^2X^2\right)\left[G^2 + G^{3/2}\coth\left(\sqrt{G}H\right)\right]}, \tag{5.28}$$

with $G = K^2 + Q^2 - 2KQ\cos\theta$. Since this integral cannot be performed analytically, we evaluate it via a numerical method. We explore the dependencies of D on the variable K, and the parameters X and H. Notice that the dimensionless correlation length X also measures the proximity of the temperature with respect to the critical temperature T_c.

In Fig. 5.4, we plot the diffusion coefficient D (scaled by $k_B T/4\pi\eta$) as a function of dimensionless wave number K for a different solvent thickness H while the correlation length is fixed to $X = 1$ (i.e., fixed temperature). In the limit of $K \ll 1$, D is almost a constant. The calculated D starts to increase

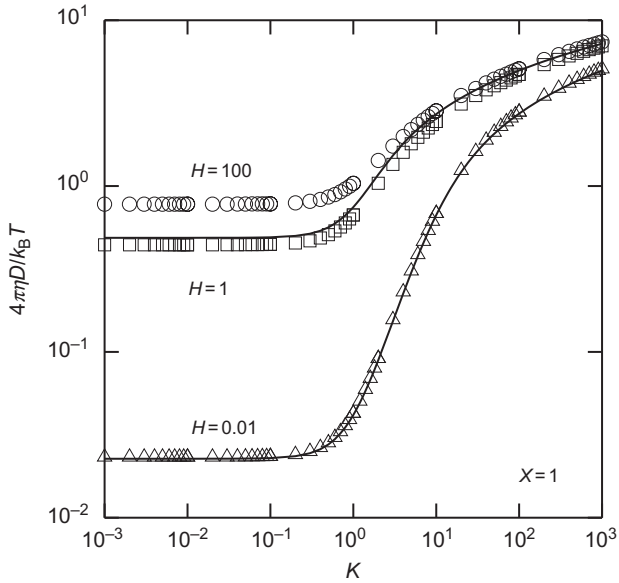

Figure 5.4 Scaled effective diffusion coefficient D as a function of K for $H = 0.01$, 1, and 100 when $X = 1$. The solid lines are from the analytical expression given in Eq. (5.29) obtained in the limit of small H.

around $K \approx 1$, and a logarithmic behavior (extracted via numerical fitting) is seen for $K \gg 1$. In this plot, we see that D becomes smaller for smaller values of H. Figure 5.5 shows the diffusion coefficient D as a function of wave number K for different X (i.e., different temperatures) while the solvent height is fixed to $H = 1$. Here D is nearly constant for $K \ll 1/X$ and follows an S-shaped curve with increasing K. Finally, a logarithmic dependence is observed for large K. We note that this logarithmic behavior for $K \gg 1/X$ is in contrast to that of 3D critical fluids given by the Kawasaki function which increases linearly with the wave number [40].

In Fig. 5.6, we explore the effect of the correlation length X on D for different values of H when $K = 10^{-3}$. The quantity X is a measure of an effective size of the correlated region formed transiently in the membrane due to thermal fluctuations. When $X \ll 1$, the diffusion coefficient D decreases only logarithmically, which is typical for a pure 2D system [22–24]. The proximity to the walls results in a loss of momentum from the membrane [29]. This leads to a rapid suppression of the velocity field within the membrane. Consequently, the values of D are smaller for smaller H. The flattening of the curves for $X \gg 1$ is due to the dominance of the X^2 terms in the numerator and denominator in Eq. (5.28). In Fig. 5.7,

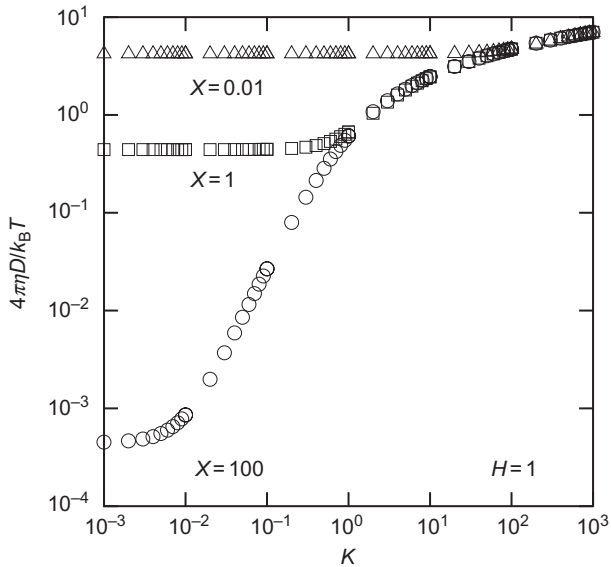

Figure 5.5 Scaled effective diffusion coefficient D as a function of K for $X = 0.01$, 1, and 100 when $H = 1$.

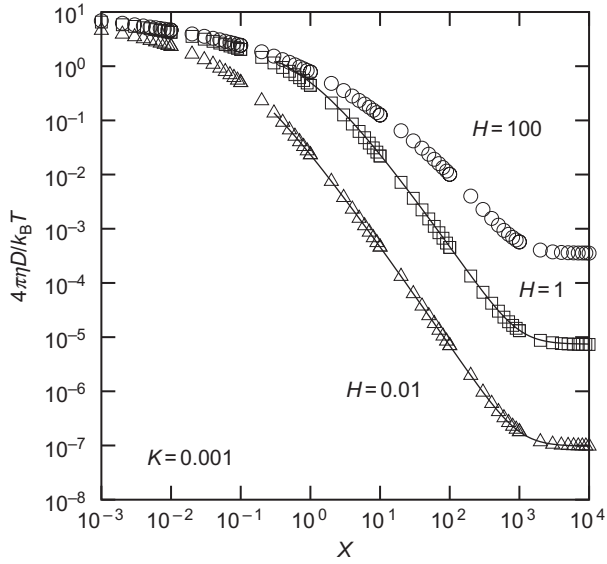

Figure 5.6 Scaled effective diffusion coefficient D as a function of X for $H=0.01$, 1, and 100 when $K=10^{-3}$. The solid lines are from the analytical expression given in Eq. (5.29) obtained in the limit of small H.

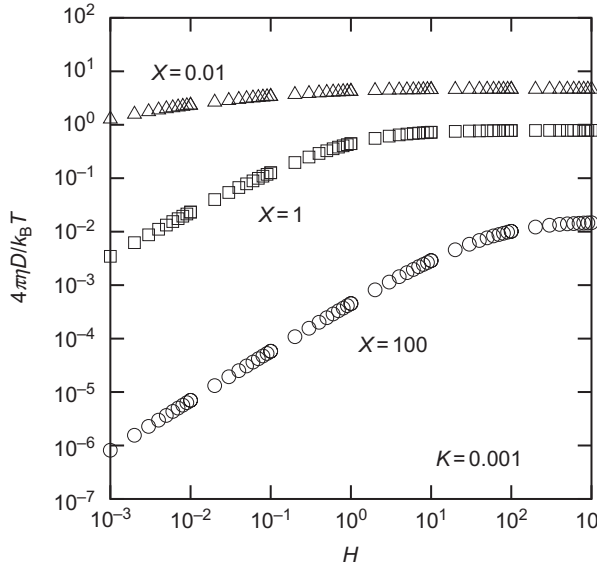

Figure 5.7 Scaled effective diffusion coefficient D as a function of H for $X=0.01$, 1, and 100 when $K=10^{-3}$.

we plot D as a function of H for different values of X when $K=10^{-3}$. Here the values of D are smaller for larger X, as it should be. In general, there is a monotonic increase of D followed by a saturation to a constant value for larger H. It is interesting to note that the crossover occurs when $H\approx X$ holds.

For confined membranes (small h), we showed in Section 2 that the general mobility tensor Eq. (5.9) reduces to $G^{\rm con}_{\alpha\beta}$ given by Eq. (5.12). In this case, one can obtain an analytical expression for the effective diffusion coefficient [32]. In terms of the dimensionless quantities K, X, and H, it is written as

$$\begin{aligned} D[K;X,H]=\frac{k_{\rm B}T}{4\pi\eta}\frac{1+K^2X^2}{2K^2X^2}\Bigg[&-\ln\left(\frac{X}{\sqrt{H}}\right)\\ &+\frac{H}{X^2}\left(1+K^2X^2\right)\ln\left(\frac{X}{\sqrt{H}(1+K^2X^2)}\right)\\ &+\frac{H\Omega}{2X^2}\ln\left(\frac{K_+^4+K_-^2+K_+^2\Omega}{\Omega-K_-^2-1}\right), \end{aligned} \tag{5.29}$$

where

$$\Omega=\sqrt{\left(K^2X^2+X^2/H-1\right)^2+4K^2X^2}, \tag{5.30}$$

and

$$K_\pm=\sqrt{K^2X^2\pm X^2/H}. \tag{5.31}$$

Equation (5.29) is plotted using solid lines in Fig. 5.4 for $H=0.01$ and 1 with $X=1$. For $H=0.01$, the analytical and numerical data coincide, giving credence to accuracy of the numerical solutions. It is seen that even for $H=1$, the agreement is still acceptable. For $H=100$, however, a significant deviation is observed (not shown), which is expected as this limit is beyond the valid range of Eq. (5.29).

The solid lines in Fig. 5.6 also represent the analytical result of Eq. (5.29). It is seen that the analytical and the numerical data points almost coincide for $H=0.01$ and 1. The agreement between the numerical result and the analytical expression is beyond the expected range of $H\ll 1$ and reaches up to $H\approx 1$, as pointed out by Stone and Ajdari [28]. Hence Eq. (5.29) is useful in analyzing the experimental data in many situations.

When the critical temperature T_c is approached from above, the correlation length diverges according to $\xi\approx|T-T_c|^{-\bar{\nu}}$, where $\bar{\nu}$ is the critical

exponent. When T_c is approached from below, on the other hand, the order parameter given by the difference in lipid compositions vanishes as $\delta\psi \approx (T_c - T)^{\bar{\beta}}$. From the experiments on model multicomponent vesicles, these critical exponents were found to have values close to $\bar{\beta} = 1/8$ and $\bar{\nu} = 1$, respectively [13]. Furthermore, the experiment on giant plasma membrane vesicles measured the critical exponent $\bar{\gamma} = 7/4$ which characterizes the critical behavior of the osmotic compressibility [15]. These static exponents seem to coincide with the exact results of the 2D Ising model [14]. The description presented in this section uses a mean-field approach, and therefore, the corresponding exponents are $\bar{\beta} = 1/2$, $\bar{\nu} = 1/2$, and $\bar{\gamma} = 1$, respectively. The discrepancies between these values are still under discussion.

3.3. Membrane as a 2D microemulsion

The role of surfactant molecules in 3D microemulsions is to reduce the surface tension at the interface between oil and water. In an analogy to 3D microemulsions, hybrid lipids (one chain unsaturated and the other saturated) act as lineactant molecules which stabilize finite-sized domains in 2D. In other words, hybrid lipids play a similar role to surfactant molecules at the interface between L_o and L_d domains. It should be also noticed that hybrid lipids form a major percentage of all naturally existing lipids [41]. Based on a simple model of hybrid lipids, Brewster *et al.* showed that finite-sized domains can be formed in equilibrium [34,35]. A subsequent model predicted that domains are even more stabilized in a system of saturated/hybrid/cholesterol lipid membranes [36,37]. Being motivated by this idea, we calculate the decay rate of concentration fluctuations when the free energy of the multicomponent membrane has the form of a 2D microemulsion.

The free-energy functional for a microemulsion includes a higher order derivative term and is expressed in terms of $\delta\psi$ as [16]

$$\mathcal{F}_{\mathrm{ME}}\{\delta\psi\} = \int \mathrm{d}\mathbf{r}\left[\frac{a}{2}(\delta\psi)^2 + \frac{c}{2}(\nabla\delta\psi)^2 + \frac{g}{2}\left(\nabla^2\delta\psi\right)^2\right], \tag{5.32}$$

with $a, g > 0$ and $c < 0$. The negative value of c creates 2D interfaces, while the term with positive g is a stabilizing term. This form of the free energy has been used previously to study coupled modulated bilayers [42,43]. As in the previous section, the decay rate of the correlation function can be split into two parts. First, the van Hove part now becomes

$$\Gamma^{(1)}_{\mathrm{ME}}[\mathbf{k}] = \Lambda k_{\mathrm{B}} T k^2 \chi^{-1}_{\mathrm{ME}}[\mathbf{k}], \tag{5.33}$$

where the static correlation function $\chi_{\mathrm{ME}}[\mathbf{k}]$ is [44]

$$\chi_{\mathrm{ME}}[\mathbf{k}] = \frac{k_{\mathrm{B}}T}{gk^4 + ck^2 + a}. \tag{5.34}$$

By defining

$$k_0^2 = -\frac{c}{2g}, \tag{5.35}$$

$$\sigma^4 = \frac{a}{g} - \left(\frac{c}{2g}\right)^2, \tag{5.36}$$

we can write the static correlation function as

$$\chi_{\mathrm{ME}}[\mathbf{k}] = \frac{k_{\mathrm{B}}T}{g\left[\left(k^2 - k_0^2\right)^2 + \sigma^4\right]}. \tag{5.37}$$

On plotting χ_{ME} as a function of k, a peak appears at $k = k_0$ followed by a $1/k^4$ decay. The width of the peak is given by σ. A lamellar phase appears when $\sigma = 0$. Notice that $c = 0$ is called the Lifshitz point at which the peak occurs for $k = 0$. Using the form of Eq. (5.37), we can write Eq. (5.33) as

$$\Gamma_{\mathrm{ME}}^{(1)}[\mathbf{k}] = \Lambda g k^2 \left[\left(k^2 - k_0^2\right)^2 + \sigma^4\right]. \tag{5.38}$$

Similar to the previous section, we next write the hydrodynamic part of the decay rate in terms of the effective diffusion coefficient $D_{\mathrm{ME}}[\mathbf{k}]$ as

$$\Gamma_{\mathrm{ME}}^{(2)}[\mathbf{k}] = k^2 D_{\mathrm{ME}}[\mathbf{k}]. \tag{5.39}$$

Using the mobility tensor given by Eq. (5.9), we can write D_{ME} as

$$D_{\mathrm{ME}}[K; K_0, \Sigma, H] = \frac{k_{\mathrm{B}}T}{4\pi^2\eta}\left[\left(K^2 - K_0^2\right)^2 + \Sigma^4\right] \times \int_0^\infty \mathrm{d}Q \int_0^{2\pi} \mathrm{d}\theta \frac{Q^3 \sin^2\theta}{\left[\left(Q^2 - K_0^2\right)^2 + \Sigma^4\right]\left[G^2 + G^{3/2}\coth\left(\sqrt{G}H\right)\right]}, \tag{5.40}$$

where $K = q/v, K_0 = q_0/v, Q = q/v, \Sigma = \sigma/v, H = hv$, and $G = K^2 + Q^2 - 2KQ\cos\theta$.

In Fig. 5.8, we plot D_{ME} as a function of K for different values of H when $K_0 = \Sigma = 1$ are fixed. When $K \ll 1$, D shows a constant value. We also observe the 2D characteristic of logarithmic behavior of D for $K \gg 1$.

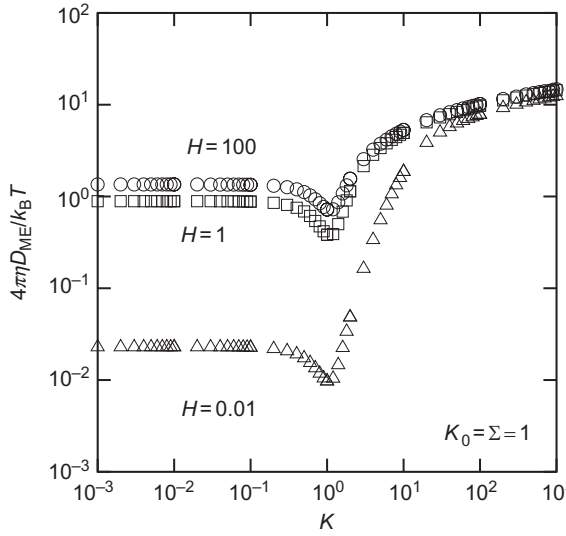

Figure 5.8 Scaled effective diffusion coefficient D_{ME} as a function of K for $H=0.01$, 1, and 100 when $K_0=\Sigma=1$.

For $K\ll 1$, the effect of the outer environment is felt with the suppression of the diffusion coefficient with smaller H. The curves almost overlap when $K\gg 1$, indicating the negligible effect of the outer environment at large wave numbers. An interesting feature of D_{ME} is the dip occurring at $K\approx K_0$ which does not exist for binary critical fluids. This can be attributed to the peak at $k=k_0$ in $\chi_{ME}[\mathbf{k}]$ [39,44]. We also note that, for 3D microemulsions, the effective diffusion coefficient varies linearly with the wave number when it is large enough [39], which is in contrast to the present 2D microemulsions.

3.4. Related works

In addition to the present theory, there are some other theoretical works on concentration fluctuations in multicomponent membranes. Using renormalization group techniques, Tserkovnyak and Nelson calculated protein diffusion in a multicomponent membrane close to a rigid substrate [45]. They pointed out that, in the vicinity of the critical point, the effective protein diffusion coefficient acquires a power-law behavior. Inaura and Fujitani first discussed concentration fluctuations in free membranes surrounded by a 3D solvent [46]. They used the mobility tensor $G^{free}_{\alpha\beta}$ in Eq. (5.10) and calculated numerically the effective diffusion coefficient.

Hence their calculation corresponds to the special case of the present theory. Haataja also discussed critical dynamics in multicomponent lipid membranes and showed that the effective diffusion coefficient exhibits a crossover from a logarithmic behavior to an algebraic dependence (inversely proportional to the correlation length) for larger length scales [47]. However, since an approximate empirical relation for the diffusion coefficient of a moving object was employed [48], his theory should be distinguished from ours. Concentration fluctuations in membranes in the absence of hydrodynamic effect was recently discussed by McConnell [49].

4. PHASE SEPARATION DYNAMICS

4.1. Domain coarsening

Although biomembranes can be regarded as 2D viscous fluids, they are not isolated pure 2D systems since lipids are coupled to the adjacent solvent. Hence it is of great interest to investigate the phase separation dynamics in such a quasi-2D liquid membrane in the presence of hydrodynamic interaction. (We use the word "quasi-2D" whenever the membrane is coupled to the bulk fluid.) To address this problem, we consider a 2D binary viscous membrane in contact with a bulk solvent. We employ a simple model in which the membrane is confined to a plane with the bulk fluid particles added above and below. In our model using DPD simulation technique, the exchange of momentum between the membrane and the bulk solvent is naturally taken into account. We particularly focus on the effect of bulk solvent on the quasi-2D phase separation.

Before explaining our simulation, let us briefly review here the general knowledge about phase separation of binary fluids following a quench [50]. The dynamic scaling hypothesis assumes that there exists a scaling regime characterized by the average domain size R that grows with time t as $R \sim t^{\alpha}$ with an universal exponent α. For 3D off-critical binary fluids, there is an initial growth by the BC process [51], followed by the Lifshitz–Slyozov (LS) evaporation–condensation process [52]; both mechanisms show a growth exponent $\alpha = 1/3$. For critical mixtures, there is an intermediate $\alpha = 1$ regime owing to hydrodynamic flow effect [53]. This is followed by a late time inertial regime of $\alpha = 2/3$ [54]. The scenario is slightly different for pure 2D systems [55]. For an off-critical mixture, it was predicted that after the initial formation of domains, they grow by the BC mechanism with a different exponent $\alpha = 1/2$ (as will be explained later), followed by a crossover to the LS mechanism which gives $\alpha = 1/3$ even in 2D. For critical mixtures, on the other hand, the initial quench produces an interconnected

structure which coarsens and then breaks up due to the interface diffusion with an exponent $\alpha = 1/2$. After the breakup processes, coarsening takes place through BC that is again characterized by the $\alpha = 1/2$ scaling [51]. These predictions were confirmed by molecular dynamics simulations in 2D [56]. The exponent $\alpha = 1/2$ was also observed in 2D lattice-Boltzmann simulations in the presence of thermal noise for a critical mixture [57].

4.2. Model and simulation technique

We use a structureless model of the 2D fluid membrane within the DPD framework [58,59]. As shown in Fig. 5.9, the 2D membrane is represented by a single layer of particles confined to a plane. In order to study phase separation, we introduce two species of particles, A and B. The bulk fluid which we call as "solvent" (S) is also represented by single particles of same size as that of the membrane particles. All particles have the same mass m.

In DPD, the interaction between any two particles, within a range r_0, is linearly repulsive. The pairwise interaction leads to full momentum conservation, which in turn brings out the correct fluid hydrodynamics. The force on a particle i is given by

$$m\frac{\mathrm{d}\mathbf{v}_i}{\mathrm{d}t} = \sum_{j\neq i}\left[\mathbf{F}_{ij}^{\mathrm{C}}\left(\mathbf{r}_{ij}\right) + \mathbf{F}_{ij}^{\mathrm{D}}\left(\mathbf{r}_{ij},\mathbf{v}_{ij}\right) + \mathbf{F}_{ij}^{\mathrm{R}}\left(\mathbf{r}_{ij}\right)\right], \tag{5.41}$$

where $\mathbf{r}_{ij} = \mathbf{r}_i - \mathbf{r}_j$ and $\mathbf{v}_{ij} = \mathbf{v}_i - \mathbf{v}_j$. Of the three types of forces acting on the particles, the conservative force on particle i due to j is $\mathbf{F}_{ij}^{\mathrm{C}} = a_{ij}\omega\left(r_{ij}\right)\hat{\mathbf{r}}_{ij}$,

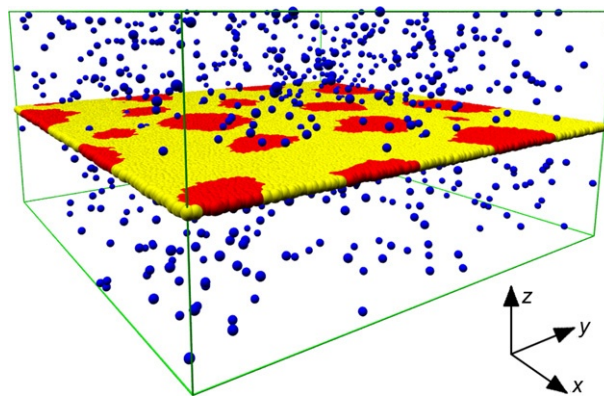

Figure 5.9 Image of the fluid membrane with the bulk fluid called solvent. The yellow (A) and red (B) particles represent the two components constituting the membrane, while blue ones (S) represent the solvent. For clarity, only a fraction of the solvent particles are shown.

where a_{ij} is an interaction strength and $\hat{\mathbf{r}}_{ij} = \mathbf{r}_{ij}/r_{ij}$ with $r_{ij} = |\mathbf{r}_{ij}|$. The second type of force is the dissipative force $\mathbf{F}_{ij}^{\mathrm{D}} = -\Gamma_{ij}\omega^2(r_{ij})(\hat{\mathbf{r}}_{ij}\cdot\mathbf{v}_{ij})\hat{\mathbf{r}}_{ij}$, where Γ_{ij} is the dissipative strength for the pair (i, j). The last is the random force $\mathbf{F}_{ij}^{\mathrm{R}} = \sigma_{ij}(\Delta t)^{-1/2}\omega(r_{ij})\zeta_{ij}\hat{\mathbf{r}}_{ij}$, where σ_{ij} is the amplitude of the random noise for the pair (i, j), and ζ_{ij} is a random variable with zero mean and unit variance which is uncorrelated for different pairs of particles and different time steps. The dissipative and random forces act as a thermostat, provided the fluctuation–dissipation theorem $\sigma_{ij}^2 = 2\Gamma_{ij}k_{\mathrm{B}}T$ is satisfied. The weight factor is chosen as $\omega(r_{ij}) = 1 - r_{ij}/r_0$ up to the cutoff radius r_0 and zero thereafter. The particle trajectories are obtained by solving Eq. (5.41) using the velocity-Verlet integrator. In the simulation, r_0 and m set the scales for length and mass, respectively, while $k_{\mathrm{B}}T$ sets the energy scale. The time is measured in units of $\tau = (mr_0^2/k_{\mathrm{B}}T)^{1/2}$. The numerical value of the amplitude of the random force is assumed to be the same for all pairs such that $\sigma_{ij} = 3.0$ $[(k_{\mathrm{B}}T)^3 m/r_0^2]^{1/4}$, and the fluid density is set as $\rho = 3.0$. We set $k_{\mathrm{B}}T = 1$ and the integration time step is chosen to be $\Delta t = 0.01\tau$.

The membrane is constructed by placing particles in the xy-plane in the middle of the simulation box (see Fig. 5.9). Owing to the structureless representation of the constituent particles, we apply an external potential so as to maintain the membrane integrity. This is done by fixing the z-coordinates of all the membrane particles. The work involves the systematic variation of the height of the simulation box starting from the pure 2D case. In the absence of solvent, we work with a 2D-box of dimensions $L_x \times L_y = 80 \times 80$ with 19,200 particles constituting the membrane. For the quasi-2D studies, we add solvent particles S above and below the membrane and increase the height of the box as $L_z = 5, 20$ and 40. For all the cases, there are 19,200 membrane particles. The largest box size ($L_z = 40$) has 748,800 solvent particles. The box with height $L_z = 40$ is found to be sufficiently large enough to prevent the finite-size effect which affects the membrane–solvent interaction. The system is then subject to periodic boundary conditions in all the three directions. For phase separation simulations, we introduce two species of membrane particles A and B. The interaction parameter between various particles are given by $a_{\mathrm{AA}} = a_{\mathrm{BB}} = a_{\mathrm{SS}} = a_{\mathrm{AS}} = a_{\mathrm{BS}} = 25$ and $a_{\mathrm{AB}} = 50$. In order to do a quench, the membrane is first equilibrated with a single component, following which a fraction of the particles are instantaneously changed to the B type.

4.3. Domain growth dynamics

First, we describe the results of the phase separation dynamics. The snapshots for A:B composition set to 70:30 (off-critical mixture) are shown in Fig. 5.10 for both pure 2D case (A) and quasi-2D case with $L_z = 40$ (B). Qualitatively,

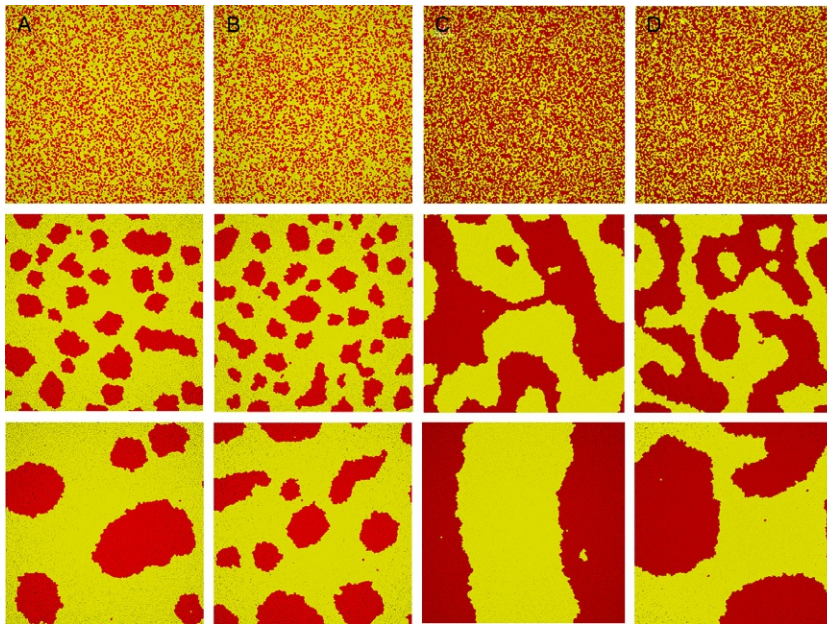

Figure 5.10 The snapshots of a 70:30 (off-critical) mixture undergoing phase separation at $t = 0$, 150, and 1000 (top to bottom) for a pure 2D (A) and quasi-2D system with $L_z = 40$ (B). The same sequences of a 50:50 (critical) mixture for a pure 2D (C) and quasi-2D system (D).

it is seen that the domains for the quasi-2D case are smaller in size when compared at the same time step. We also monitor the average domain size $R(t)$ which can be obtained from the total interface length $L(t)$ between the two components. This is because $R(t)$ and $L(t)$ are related by $L(t) = 2\pi N(t)$ $R(t)$, where $N(t)$ is the number of domains. The area occupied by the B-component is given by $\mathcal{A} = \pi N(t) R^2(t)$ which is a conserved quantity. Then we have

$$R(t) = 2\mathcal{A}/L(t). \tag{5.42}$$

When the domain size grows as $R \sim t^{\alpha}$, one has $L \sim t^{-\alpha}$ and $N \sim t^{-2\alpha}$. The domain size $R(t)$ for 70:30 mixture is shown in Fig. 5.11. In this plot, an average over 10 independent trials has been taken. It can be seen that the pure 2D case has a growth exponent $\alpha = 1/2$. Upon the addition of solvent, we observe that the exponent shifts to a lower value of $\alpha = 1/3$. This exponent is reminiscent of the phase separation dynamics of an off-critical mixture in 3D. By systematically increasing the amount of solvent in the system by changing the height L_z, we can see a clear deviation from the pure 2D

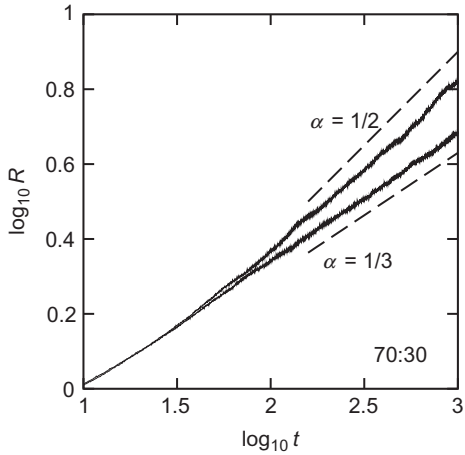

Figure 5.11 The average domain size R as a function of time t for a 70:30 off-critical mixture. The upper curve is the pure 2D case showing an $\alpha = 1/2$ scaling, and the lower curve is the quasi-2D case when $L_z = 40$ showing a distinct $\alpha = 1/3$ scaling.

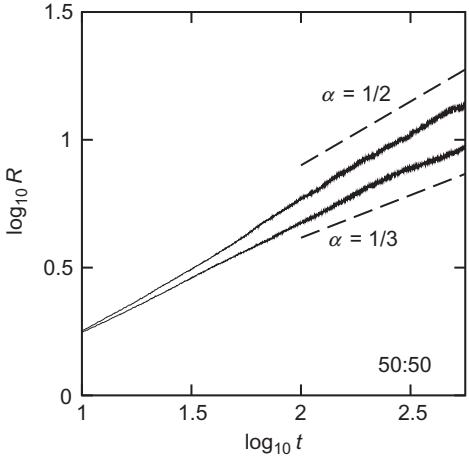

Figure 5.12 The average domain size R as a function of time t for a 50:50 critical mixture. The upper curve is the pure 2D case showing an $\alpha = 1/2$ scaling, and the lower curve is the quasi-2D case when $L_z = 40$ showing a distinct $\alpha = 1/3$ scaling.

behavior (not shown). There is no further change if L_z is increased beyond 40. A larger system size $L_x \times L_y = 200 \times 200$ also produced the same scaling for the pure 2D case, which demonstrates that finite-size effects are small.

In Fig. 5.12, we show the result for a component ratio of 50:50 (critical mixture), whereas the corresponding patterns are given in Fig. 5.10C and D for 2D and quasi-2D cases, respectively. In this case, the growth exponent

for the pure 2D case is less obvious owing to rapid coarsening of the domains. However, by simulating a bigger system 200×200 with the same areal density, an $\alpha = 1/2$ exponent is indeed obtained. Similar to the off-critical case, the growth of the domains is slowed down by the addition of solvent and the exponent is reduced to $\alpha = 1/3$. These results indicate that solvent is responsible for slowing down the growth dynamics.

The observed exponent $\alpha = 1/2$ in pure 2D systems can be explained in terms of the BC mechanism [55]. From dimensional analysis, the 2D diffusion coefficient of the domain is given by $D_2 \sim k_B T/\eta$, where η is the membrane 2D viscosity. Using the relation

$$R^2 \sim D_2 t \sim \left(\frac{k_B T}{\eta}\right) t, \tag{5.43}$$

we find $R \sim t^{1/2}$. For 3D systems, on the other hand, the diffusion coefficient of the droplet is inversely proportional to its size, $D_3 \sim 1/R$, a well-known Stokes–Einstein relation. Hence the BC mechanism in 3D gives rise to an exponent $\alpha = 1/3$. (In general, the exponent is $\alpha = 1/d$, where d is the space dimension.) The change in the exponent from $\alpha = 1/2$ to $1/3$ due to the addition of solvent implies the crossover from 2D to 3D behaviors of the phase separation dynamics even though the lateral coarsening takes place only within the 2D geometry. Notice that the LS mechanism shows an exponent of $\alpha = 1/3$ in both 2D and 3D. We thus conclude that our simulations are still in the early time of the coarsening dynamics.

4.4. Correlated diffusion

In order to justify our argument, it is necessary to examine the size dependence of the domain diffusion coefficient in quasi-2D systems. This can be calculated by tracking the mean-squared displacement of domains of various radii. The equivalent information can be more efficiently obtained by calculating the two-particle longitudinal coupling diffusion coefficient in a single component membrane rather than in a binary system.

Consider a pair of particles separated by a 2D vector $\mathbf{r}$, undergoing diffusion in the fluid membrane. The two-particle mean-squared displacement is given by [25,26]

$$\left\langle \Delta r_\alpha^k \Delta r_\beta^l \right\rangle = 2 D_{\alpha\beta}^{kl}(\mathbf{r}) t, \tag{5.44}$$

where Δr_α^k is the displacement of the particle $k(=1,2)$ along the axis $\alpha(=x, y)$, and $D_{\alpha\beta}^{kl}$ is the diffusion tensor giving self-diffusion when $k = l$ and the

coupling between them when $k \neq l$. The x-axis is defined along the line connecting a pair of particles 1 and 2, that is, $\mathbf{r} = r\hat{x}$. Hence, we have $D^{12}_{xy} = 0$ by symmetry. The longitudinal coupling diffusion coefficient, $D_{\mathrm{L}}(r) = D^{12}_{xx}(r\hat{x})$, gives the coupled diffusion along the line of centers of the particles.

We first describe the analytical expression of $D_{\mathrm{L}}(r)$ for the free membrane case, which can be essentially obtained from Eq. (5.11) (see Ref. [17] for details). Using the Einstein relation for over-damped dynamics, we obtain

$$D_{\mathrm{L}}^{\mathrm{free}}(r) = \frac{k_{\mathrm{B}}T}{4\pi\eta}\left[-\frac{2}{\nu^2 r^2} + \frac{\pi \mathbf{H}_1(\nu r)}{\nu r} - \frac{\pi Y_1(\nu r)}{\nu r}\right]. \tag{5.45}$$

At short distances $r \ll \nu^{-1}$, the asymptotic form of the above expression becomes

$$D_{\mathrm{L}}^{\mathrm{free}}(r) \approx \frac{k_{\mathrm{B}}T}{4\pi\eta}\left[\ln\left(\frac{2}{\nu r}\right) - \gamma + \frac{1}{2}\right], \tag{5.46}$$

where $\gamma = 0.5772\ldots$ is Euler's constant. At large inter-particle separations $r \gg \nu^{-1}$, on the other hand, Eq. (5.45) reduces to

$$D_{\mathrm{L}}^{\mathrm{free}}(r) \approx \frac{k_{\mathrm{B}}T}{2\pi\eta\nu r} = \frac{k_{\mathrm{B}}T}{4\pi\eta_{\mathrm{s}} r}, \tag{5.47}$$

showing the asymptotic $1/r$ decay which reflects the 3D nature of this limit. Notice that Eq. (5.47) depends only on the solvent viscosity η_{s} but not on the membrane viscosity η any more.

In Fig. 5.13, we plot the measured longitudinal coupling diffusion coefficient D_{L} as a function of 2D distance r. In these simulations, we have worked with only single component membranes with the same system sizes and number of particles as those used for the phase separation simulations. We have also taken average over 20 independent trials. In the pure 2D case without any solvent, D_{L} shows a logarithmic dependence on r. This is consistent with Eq. (5.46) obtained when the coupling between the membrane and solvent is very weak so that the membrane can be regarded almost as a pure 2D system. Using Eq. (5.46) as an approximate expression, we get from the fitting as $k_{\mathrm{B}}T/4\pi\eta \approx 0.89 \times 10^{-2}$ and $\nu^{-1} \approx 20$. In an ideal case, the SD screening length should diverge due to the absence of solvent. The obtained finite value for ν^{-1} is roughly set by the half of the system size in the simulation.

When we add solvent ($L_z = 40$), the D_{L} is decreased and no longer behaves logarithmically. In this case, we use the full expression Eq. (5.45) for the fitting and obtained $k_{\mathrm{B}}T/4\pi\eta \approx 1.35 \times 10^{-2}$ and $\nu^{-1} \approx 1$. In the above

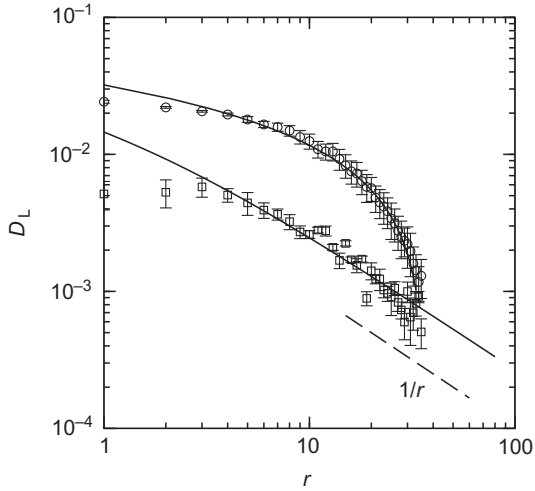

Figure 5.13 Longitudinal coupling diffusion D_L as a function of particle separation r. The upper circles are data for the pure 2D case. The lower squares correspond to the case with solvent when $L_z = 40$. The upper solid line is the fit by Eq. (5.46), and the lower solid line is the fit by Eq. (5.45). The dashed line shows the $1/r$ dependence.

two fits, we have neglected the first two points as they lie outside the range of validity, $r \gg 1$, of Eq. (5.45). Since $\nu^{-1} \approx 1$ when the solvent is present, the data shown in Fig. 5.13 are in the crossover region, $r \gtrsim \nu^{-1}$, showing an approach toward the asymptotic $1/r$ dependence as in Eq. (5.47). Hence we conclude that the solvent brings in the 3D hydrodynamic property to the diffusion in membranes. This is the reason for the exponent $\alpha = 1/3$ in the phase separation dynamics and justifies that it is mainly driven by BC mechanism.

In our simulations, the membrane and the solvent have very similar viscosities. This sets the SD length scale to be of the order of unity (in units of particle size), which is consistent with the value $\nu^{-1} \approx 1$ obtained from the fitting. As explained above, the fit also provides the 2D membrane viscosity as $\eta \approx 6$, and hence we obtain as $\eta_s \approx 3$. In real biomembranes sandwiched by water, the value of the SD length is much larger than the lipid size and is in the order of submicron scale [23]. Hence the 3D nature of hydrodynamics should be observed for large enough domains [60].

For confined membranes, on the other hand, the appropriate mobility tensor is $G^{\rm con}_{\alpha\beta}$ given by Eq. (5.12). In this case, the longitudinal coupling diffusion coefficient can be obtained as [17]

$$D_{\rm L}^{\rm con}(r) = \frac{k_{\rm B}T}{2\pi\eta}\left[\frac{1}{\kappa^2 r^2} - \frac{K_1(\kappa r)}{\kappa r}\right], \tag{5.48}$$

where $K_1(z)$ is modified Bessel function of the second kind (see also Eq. 13). At short distances $r \ll \kappa^{-1}$, we have

$$D_{\mathrm{L}}^{\mathrm{con}}(r) \approx \frac{k_{\mathrm{B}}T}{4\pi\eta}\left[\ln\left(\frac{2}{\kappa r}\right) - \gamma + \frac{1}{2}\right], \tag{5.49}$$

which is almost identical to Eq. (5.46) except ν is replaced now by κ. At long distances $r \gg \kappa^{-1}$, on the other hand, we get

$$D_{\mathrm{L}}^{\mathrm{con}}(r) \approx \frac{k_{\mathrm{B}}T}{2\pi\eta\kappa^2 r^2} = \frac{k_{\mathrm{B}}Th}{4\pi\eta_{\mathrm{s}} r^2}, \tag{5.50}$$

which exhibits a $1/r^2$ dependence. This is in contrast to Eq. (5.47). Repeating the similar scaling argument, we predict that, in the presence of walls, the domain growth exponent should be $\alpha = 1/4$ within the BC mechanism. A similar simulation with two confining hard walls is required as a next step. In biological systems, the above situation with solid walls can be relevant because the cell membranes are strongly anchored to the underlying cytoskeleton or are tightly adhered to other cells.

4.5. Related works

We mention here several related works on the phase separation dynamics below the transition temperature. Veatch and Keller observed the kinetics of domain growth on ternary vesicles as presented in Fig. 5.14 [9]. For a

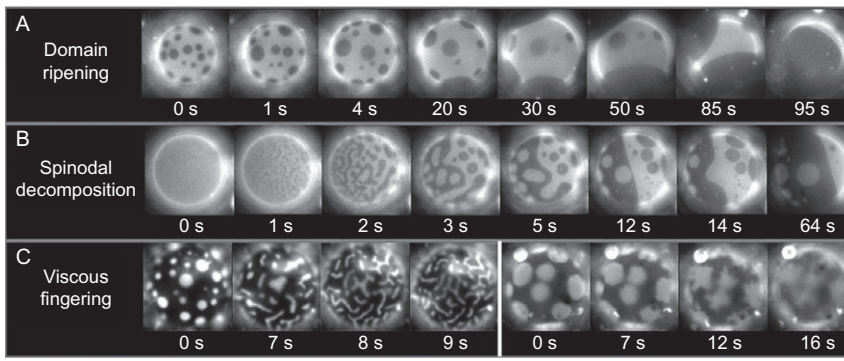

Figure 5.14 Phase separation dynamics on ternary giant vesicles. (A) Brownian coagulation observed for 1:1 DOPC/DPPC + 25% Chol., (B) spinodal decomposition observed for 1:1 DOPC/DPPC + 35% Chol., (C) viscous fingering observed for 1:9 DOPC/DPPC + 25% Chol. (left series) and 1:1 DOPC/DMPC + 25% Chol. (right series). *Adapted from Ref. [9].*

vesicle with an off-critical composition, dark circular domains grow by colliding and coalescing with each other rather than through the LS evaporation–condensation process (Fig. 5.14A). When the composition is nearly critical, spinodal decomposition takes place when the temperature is decreased through transition point (Fig. 5.14B). For a highly asymmetric composition as in Fig. 5.14C, striped domains are observed when the temperature is raised; possibly viscous fingering.

The domain growth exponent α was first measured by Saeki *et al.* for ternary vesicles composed of DOPC, DPPC, and cholesterol [61]. They indeed observed a power-law behavior and reported a rather small value $\alpha = 0.15$. The reason for this slow dynamics was partially attributed to the curvature of the domain portion. Subsequently, Yanagisawa and some of the present authors found that the domain coarsening processes are classified into two types, that is, normal coarsening and trapped coarsening [62]. In the former case, the domains having flat circular shape grow through BC process, although the growth exponent was found to be $\alpha = 2/3$. For the trapped coarsening, on the other hand, the domain growth is suppressed at a certain domain size because the repulsive inter-domain interactions obstruct the coalescence of domains. A two-color imaging technique of the trapped domains revealed that this repulsive interactions are induced by the budding of domains. By observing the motion of domains, they also found that each domain is attracted toward the largest one following the flow around it. This is a strong indication of the hydrodynamic interactions acting between the domains.

As for computer simulations, Laradji and Kumar performed a DPD study on phase separation dynamics in both two-component vesicles and open membranes using a coarse-grained model for the membrane lipids [63–65]. In their model, the self-assembly of a bilayer in the presence of solvent is naturally taken into account. For off-critical case, they obtained an exponent $\alpha \approx 0.3$ which is in good agreement with our simulation result, $\alpha \approx 1/3$. Similar to our observation, they also reported that the BC process takes place rather than the LS evaporation–condensation process. However, when the excess area of a vesicle is large enough, domains are no more flat and reshape into caps. In such a case, Eq. (5.42) is not valid and it is more convenient to measure the interface length $L(t)$. According to their simulation, it scales as $L(t) \sim t^{-0.4}$, indicating that the interfacial length decreases faster as compared to the case of small excess area. For membranes with critical composition, the growth exponent was found to be $\alpha \approx 0.5$ for both vesicles and open membranes. This value is in contrast to our result $\alpha \approx 1/3$ as shown in Fig. 5.12. In Fig. 5.15, we

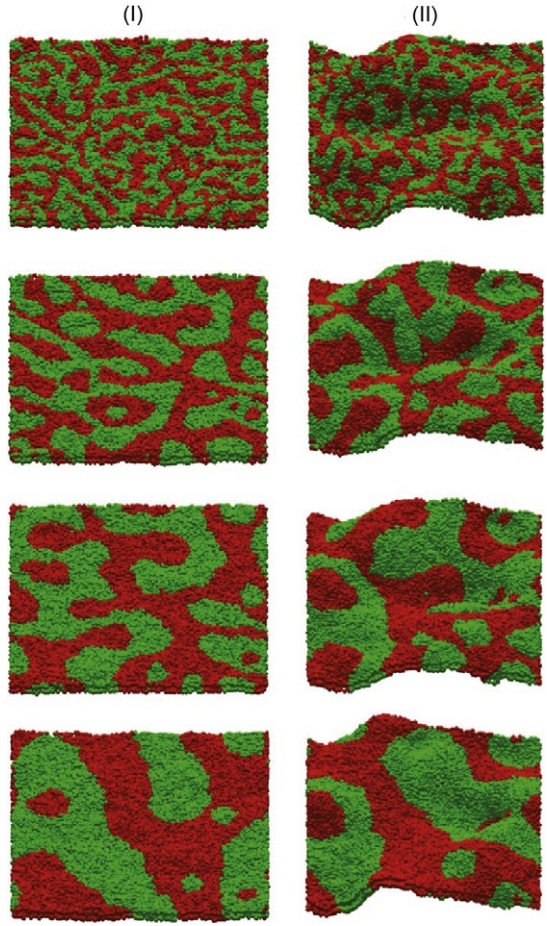

Figure 5.15 The snapshots for a 50:50 critical mixture undergoing phase separation for open membranes with different projected areas (I and II). Adapted from Ref. [64].

present a sequence of spinodal decomposition for open membranes obtained from their simulation. One of the differences between their simulation and ours is that the membrane is not allowed to exhibit out-of-plane fluctuations in our case. In their subsequent work, the effect of asymmetry in the bilayer lipid composition was studied [66]. Notice that flip-flop events are extremely rare in their simulation. This asymmetry sets a spontaneous curvature for domains which are capped. Interestingly, they found that the coupling between the spontaneous curvature and composition effectively leads to micro-phase separation. The observed scaling behavior was $L(t) \sim t^{-0.13}$, indicative of a

logarithmic growth. Obviously, such a bilayer nature of fluid membranes is not taken into account in our simulation.

Camley *et al.* [67,68] and Fan *et al.* [69] performed numerical simulations of 2D version of model H using the mobility tensor of Eq. (5.10) for free membranes. The basic formulation of this model is given by that described in Section 3.1 except that the free-energy functional in Eq. (5.14) is replaced with

$$\mathcal{F}\{\psi\} = \int d\mathbf{r}\left[\frac{a}{2}\psi^2 + \frac{1}{4}\psi^4 + \frac{c}{2}(\nabla\psi)^2\right], \tag{5.51}$$

where $a<0$ is now negative in order to study the domain growth below the transition temperature. In the dynamical equations, Camley *et al.* included Gaussian white thermal noise terms which are distributed with variances set by the fluctuation–dissipation theorem [67,68]. By using reasonable parameter values, they were almost successful in reproducing the experimentally observed pattern evolution given in Fig. 5.14B. For the domain growth law, it was pointed out that the scaling behavior $R\sim t^{\alpha}$ would hold only when $R\ll v^{-1}$ or $R\gg v^{-1}$ because it requires the fact that R is the only relevant length scale.

For off-critical mixtures, there are at least two coarsening mechanism in this model: BC process and LS evaporation–condensation process, as mentioned before. The LS mechanism is essentially driven by the line tension λ between coexisting phases, and the corresponding growth law is given by [50]

$$R\sim(\Lambda\lambda t)^{1/3}, \tag{5.52}$$

where Λ is the kinetic coefficient given in Eq. (5.15). Notice that this exponent $\alpha=1/3$ does not depend on the dimensionality of the system. (In 3D, for example, the line tension λ is replaced with a surface tension.) On the other hand, the BC mechanism leads to $\alpha=1/2$ for $R\ll v^{-1}$ and $\alpha=1/3$ for $R\gg v^{-1}$, as we have discussed in detail. All these different scaling regimes have been confirmed by their numerical simulation [68], in agreement with our DPD simulation.

For critical mixtures, however, the results are rather complex. Figure 5.16 shows the time evolution of the phase-separated patterns for a mixture of critical composition [69]. Comparing Fig. 5.16E and F, for example, we notice that the morphologies and sizes of the elongated domains have changed considerably, whereas more isotropic ones remain almost the same. As a result, isolated circular domains coarsen slower than elongated

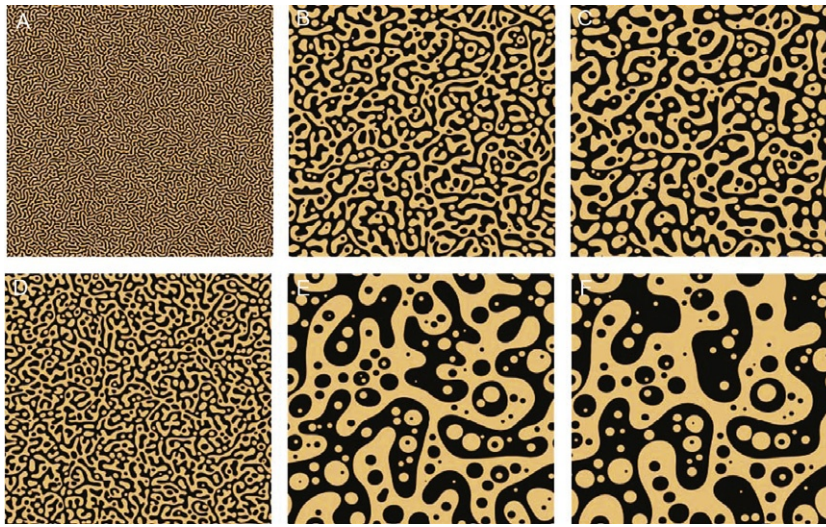

Figure 5.16 Time sequences of concentration maps during spinodal decomposition for different combinations of membrane and solvent viscosities (A–C and D–F). Time increases from left to right. Adapted from Ref. [69].

ones. From this observation together with quantitative analysis, they concluded that dynamical scaling breaks down since a single length scale cannot represent the domain distribution for different times [68,69]. Such a violation of the scaling behavior was reported before for pure 2D binary fluids [70,71]. Nevertheless, Camley *et al.* also found a region of apparent scaling where $\alpha = 1/2$ holds [68]. Although this may not be a universal feature, the power-law behavior seems to appear due to the competition between thermal and hydrodynamic effects. Furthermore, even a value close to $\alpha = 1/3$ was observed when the kinetic coefficient Λ is large [68]. This is what they call the "Cahn-Hilliard" regime in which bulk diffusion described by Λ is dominant. As a whole, the domain coarsening in critical mixtures seems to be far from universal and may dependent on the membrane viscosity.

In some other models, membranes undergoing simultaneously a phase separation and permanent exchange of lipids with the surrounding medium were considered [72,73]. For example, Foret proposed the following dynamical equation in the absence of flow [74]

$$\frac{\partial \psi}{\partial t} = \Lambda \nabla^2 \frac{\delta \mathcal{F}}{\delta \psi} - \gamma \left(\psi - \bar{\psi} \right), \tag{5.53}$$

where γ is the typical exchange rate, $\bar{\psi}$ is the average value of ψ, and $\mathcal{F}$ is given by Eq. (5.51). This equation should be contrasted with Eq. (5.15). It is interesting to note that the above equation also describes the dynamics of block copolymer systems which undergo micro-phase separation [75]. It is well known for block copolymers that the domain growth will eventually stop, and the domain size reaches a stationary value. Hence Eq. (5.53) gives rise to finite-sized raft domains in equilibrium. We point out here that 2D microemulsion discussed in Section 3.3 also exhibits a micro-phase separation below the transition temperature. Gómez *et al.* proposed a similar model in which only cholesterol is recycled [76,77]. As a generalization of these models, Fan *et al.* discussed the influence of nonequilibrium lipid transport, membrane compartmentalization, and membrane proteins on the phase separation dynamics [78–80]. Recently, micro-phase separation in nonequilibrium membrane was discussed in Ref. [81]. It should be noted, however, that the hydrodynamic effect is not taken into account in these models.

5. CONCLUSION AND OUTLOOK

In this chapter, we have discussed the dynamics of heterogeneity in multicomponent fluid membranes particularly focusing on hydrodynamic effects. For membranes above the transition temperature, we have investigated the kinetics of critical concentration fluctuations in two-component mixtures. Based on the time-dependent Ginzburg–Landau approach with full hydrodynamics, the wave number dependence of the effective diffusion coefficient was calculated as a function of the temperature and/or the thickness of the bulk fluid. For membranes below the transition temperature, we have discussed the effects of an embedding bulk solvent on the phase separation dynamics using DPD simulations. We have shown that the presence of a bulk fluid alters the domain growth exponent from that of 2D to 3D, indicating the significant role played by the membrane–solvent coupling. We further demonstrated that quasi-2D phase separation proceeds by the BC mechanism which reflects the 3D nature of the bulk solvent.

Even though the models presented in this chapter capture the essential physics, they are simplistic in several respects. The bending stiffness of typical membranes is of the order of $10k_BT$ which may be not always large enough to neglect the out-of-plane displacements of the membrane. The dynamics

of out-of-plane fluctuations of a homogeneous membrane was previously studied by Levine and MacKintosh [82]. It is worthwhile to comment that the presence of a substrate or the second membrane would suppress out-of-plane membrane fluctuations [83,84]. In our treatment, we have also neglected the effects of membrane curvature which can be significant when the radius of curvature becomes close to the hydrodynamic screening length. Henle *et al.* considered the diffusion of a point object on a spherically closed membrane [85,86]. The extension of this work to finite-sized objects is an interesting but difficult proposition.

In some theories, viscoelasticity of an infinitely large flat membrane has been considered [87,88]. Although it turned out that membranes are purely viscous in the latest report [89], their experimental technique using particle tracking microrheology provides us with a new clue to investigate the dynamical responses of lipid bilayers coupled to the surrounding environments. Recently, viscoelasticity of phospholipid Langmuir monolayers in a liquid-condensed phase was measured using active microrheology technique [90]. From our point of view, however, the viscoelasticity of the surrounding media is more important for large-scale dynamics in membranes. This is indeed the case according to the recent work by Granek who calculated the frequency-dependent transverse fluctuations of a membrane surrounded by viscoelastic media [91]. Currently, we are investigating the lateral dynamics in a purely viscous lipid membrane surrounded by viscoelastic media whose viscosity is a frequency-dependent one $\eta_s[\omega]$ [92]. For example, the frequency-dependent membrane mobility tensor is obtained as

$$G_{\alpha\beta}[\mathbf{k},\omega] = \frac{1}{\eta k^2 + 2\eta_s[\omega]k' \coth(k'h) + i\omega\rho}\left(\delta_{\alpha\beta} - \frac{k_\alpha k_\beta}{k^2}\right), \tag{5.54}$$

where

$$k' = k\left(1 + \frac{i\omega\rho_s}{\eta_s[\omega]k^2}\right)^{1/2}. \tag{5.55}$$

In the above, ρ and ρ_s are the densities of the membrane and solvent, respectively. In the limit of $\omega \to 0$, these expressions reduce to Eq. (5.9). Using Eq. (5.54), we can show that the mean square displacement of a disk embedded in the membrane exhibits an anomalous diffusion [92]. An useful relation which connects the mean square displacement and the solvent modulus is obtained.

ACKNOWLEDGMENTS

We thank D. Andelman, H. Diamant, Y. Fujitani, G. Gompper, T. Hamada, Y. Hirose, T. Kato, P. B. S. Kumar, S. L. Keller, C.-Y. D. Lu, N. Oppenheimer, and Y. Sakuma for useful discussions. This work was supported by KAKENHI (Grant-in-Aid for Scientific Research) on Priority Area "Soft matter physics" and Grant No. 21540420 from the MEXT of Japan. This work was also supported by the JSPS Core-to-Core Program "International research network for nonequilibrium dynamics of soft matter."

REFERENCES

[1] B. Alberts, A. Johnson, P. Walter, J. Lewis, M. Raff, Molecular Biology of the Cell, Garland Science, New York, 2008.
[2] R. Lipowsky, E. Sackmann, Structure and Dynamics of Membranes, Elsevier, Amsterdam, 1995.
[3] K. Simons, E. Ikonen, Functional rafts in cell membranes, Nature 387 (1997) 569–572.
[4] L.J. Pike, Rafts defined: a report on the Keystone symposium on lipid rafts and cell function, J. Lipid Res. 47 (2006) 1597–1598.
[5] M. Leslie, Do lipid rafts exist? Science 334 (2011) 1046–1047.
[6] J. Fan, M. Sammalkorpi, M. Haataja, Formation and regulation of lipid microdomains in cell membranes: theory, modeling and speculation, FEBS Lett. 584 (2010) 1678–1684.
[7] C. Eggeling, C. Ringemann, R. Medda, G. Schwarzmann, K. Sandhoff, S. Polyakova, V.N. Belov, B. Hein, C. von Middendorff, A. Schönle, S.W. Hell, Direct observation of the nanoscale dynamics of membrane lipids in a living cell, Nature 457 (2009) 1159–1162.
[8] S.L. Veatch, S.L. Keller, Organization in lipid membranes containing cholesterol, Phys. Rev. Lett. 89 (2002) 268101.
[9] S.L. Veatch, S.L. Keller, Separation of liquid phases in giant vesicles of ternary mixtures of phospholipids and cholesterol, Biophys. J. 85 (2003) 3074–3083.
[10] S.L. Veatch, S.L. Keller, Miscibility phase diagrams of giant vesicles containing sphingomyelin, Phys. Rev. Lett. 94 (2005) 148101.
[11] S.L. Veatch, S.L. Keller, Seeing spots: complex phase behavior in simple membranes, Biochim. Biophys. Acta 1746 (2005) 172–185.
[12] S.L. Veatch, O. Soubias, S.L. Keller, K. Gawrisch, Critical fluctuations in domain forming lipid mixtures, Proc. Natl. Acad. Sci. U.S.A. 104 (2007) 17650–17655.
[13] A.R. Honerkamp-Smith, P. Cicuta, M. Collins, S.L. Veatch, M. Schick, M. den Nijs, S.L. Keller, Line tensions, correlation lengths and critical exponents in lipid membranes near critical points, Biophys. J. 95 (2008) 236–246.
[14] L. Onsager, Crystal statistics: a two-dimensional model with an order-disorder transition, Phys. Rev. 65 (1944) 117–149.
[15] S.L. Veatch, P. Cicuta, P. Sengupta, A. Honerkamp-Smith, D. Holowka, B. Baird, Critical fluctuations in plasma membrane vesicles, ACS Chem. Biol. 3 (2008) 287–293.
[16] G. Gompper, M. Schick, Self-assembling Amphiphilic Systems, Academic, New York, 1994.
[17] S. Ramachandran, S. Komura, K. Seki, G. Gompper, Dynamics of a polymer chain confined in a membrane, Eur. Phys. J. E 34 (2011) 46.
[18] K. Seki, S. Ramachandran, S. Komura, Diffusion coefficient of an inclusion in a liquid membrane supported by a solvent of arbitrary thickness, Phys. Rev. E 84 (2011) 021905.
[19] L.D. Landau, E.M. Lifshitz, Fluid Mechanics, Pergamon Press, Oxford, 1987.
[20] D.K. Lubensky, R.E. Goldstein, Hydrodynamics of monolayer domains at the air-water interface, Phys. Fluids 8 (1996) 843–854.

[21] Th.M. Fischer, The drag on needles moving in a Langmuir monolayer, J. Fluid Mech. 498 (2004) 123–137.
[22] P.G. Saffman, M. Delbrück, Brownian motion in biological membranes, Proc. Natl. Acad. Sci. U.S.A. 72 (1975) 3111–3113.
[23] P.G. Saffman, Brownian motion of thin sheets of viscous fluid, J. Fluid Mech. 73 (1976) 593–602.
[24] B.D. Hughes, B.A. Pailthorpe, L.R. White, The translational and rotational drag on a cylinder moving in a membrane, J. Fluid Mech. 110 (1981) 349–372.
[25] N. Oppenheimer, H. Diamant, Correlated diffusion of membrane proteins and their effect on membrane viscosity, Biophys. J. 96 (2009) 3041–3049.
[26] N. Oppenheimer, H. Diamant, Correlated dynamics of inclusions in a supported membrane, Phys. Rev. E 82 (2010) 041912.
[27] E. Evans, E. Sackmann, Translational and rotational drag coefficients for a disk moving in a liquid membrane associated with a rigid substrate, J. Fluid Mech. 194 (1988) 553–561.
[28] H. Stone, A. Ajdari, Hydrodynamics of particles embedded in a flat surfactant layer overlying a subphase of finite depth, J. Fluid Mech. 369 (1998) 151–173.
[29] K. Seki, S. Komura, Brownian dynamics in a thin sheet with momentum decay, Phys. Rev. E 47 (1993) 2377–2383.
[30] S. Komura, K. Seki, Diffusion constant of a polymer chain in biomembranes, J. Phys. II 5 (1995) 5–9.
[31] S. Ramachandran, S. Komura, M. Imai, K. Seki, Drag coefficient of a liquid domain in a two-dimensional membrane, Eur. Phys. J. E 31 (2010) 303–310.
[32] K. Seki, S. Komura, M. Imai, Concentration fluctuations in binary fluid membranes, J. Phys. Condens. Matter 19 (2007) 072101.
[33] S. Ramachandran, S. Komura, K. Seki, M. Imai, Hydrodynamic effects on concentration fluctuations in multicomponent membranes, Soft Matter 7 (2011) 1524–1531.
[34] R. Brewster, P.A. Pincus, S.A. Safran, Hybrid lipids as a biological surface-active component, Biophys. J. 97 (2009) 1087–1094.
[35] R. Brewster, S.A. Safran, Line active hybrid lipids determine domain size in phase separation of saturated and unsaturated lipids, Biophys. J. 98 (2010) L21–L23.
[36] T. Yamamoto, R. Brewster, S.A. Safran, Chain ordering of hybrid lipids can stabilize domains in saturated/hybrid/cholesterol lipid membranes, Europhys. Lett. 91 (2010) 28002.
[37] T. Yamamoto, S.A. Safran, Line tension between domains in multicomponent membranes is sensitive to degree of unsaturation of hybrid lipids, Soft Matter 7 (2011) 7021–7033.
[38] P.M. Chaikin, T.C. Lubensky, Principles of Condensed Matter Physics, Cambridge University Press, Cambridge, 1995.
[39] M. Nonomura, T. Ohta, Decay rate of concentration fluctuations in microemulsions, J. Chem. Phys. 110 (1999) 7516–7523.
[40] K. Kawasaki, Kinetic equations and time correlation functions of critical fluctuations, Ann. Phys. 61 (1970) 1–56.
[41] G. van Meer, D. Voelker, G. Feigenson, Membrane lipids: where they are and how they behave, Nat. Rev. Mol. Cell Biol. 9 (2008) 112–124.
[42] Y. Hirose, S. Komura, D. Andelman, Coupled modulated bilayers: a phenomenological model, Chemphyschem 10 (2009) 2839–2846.
[43] Y. Hirose, S. Komura, D. Andelman, Concentration fluctuations and phase transitions in coupled modulated bilayers, submitted.
[44] M. Teubner, R. Strey, Origin of the scattering peak in microemulsions, J. Chem. Phys. 87 (1987) 3195–3200.

[45] Y. Tserkovnyak, D.R. Nelson, Conditions for extreme sensitivity of protein diffusion in membranes to cell environments, Proc. Natl. Acad. Sci. U.S.A. 103 (2006) 15002–15007.
[46] K. Inaura, Y. Fujitani, Concentration fluctuation in a two-component fluid membrane surrounded with three-dimensional fluids, J. Phys. Soc. Jpn. 77 (2008) 114603.
[47] M. Haataja, Critical dynamics in multicomponent lipid membranes, Phys. Rev. E 80 (2009) 020902.
[48] E.P. Petrov, P. Schwille, Translational diffusion in lipid membranes beyond the Saffman-Delbrück approximation, Biophys. J. 94 (2008) L41–L43.
[49] H. McConnell, Composition fluctuations, correlated response, and protein solvation in membranes, J. Chem. Phys. 132 (2010) 205102.
[50] A.J. Bray, Theory of phase-ordering kinetics, Adv. Phys. 51 (2002) 481–587.
[51] K. Binder, D. Stauffer, Theory for the slowing down of the relaxation and spinodal decomposition of binary mixtures, Phys. Rev. Lett. 33 (1974) 1006–1009.
[52] E.M. Lifshitz, L.P. Pitaevskii, Physical Kinetics, Pergamon Press, Oxford, 1981.
[53] E.D. Siggia, Late stages of spinodal decomposition in binary mixtures, Phys. Rev. A 20 (1979) 595–605.
[54] H. Furukawa, Effect of inertia on droplet growth in a fluid, Phys. Rev. A 31 (1995) 1103–1108.
[55] M.S. Miguel, M. Grant, J.D. Gunton, Phase separation in two-dimensional binary fluids, Phys. Rev. A 31 (1985) 1001–1005.
[56] P. Ossadnik, M.F. Gyure, H.E. Stanley, S.C. Glotzer, Molecular dynamics simulation of spinodal decomposition in a two-dimensional binary fluid mixture, Phys. Rev. Lett. 72 (1994) 2498.
[57] G. Gonnella, E. Orlandini, J.M. Yeomans, Phase separation in two-dimensional fluids: the role of noise, Phys. Rev. E 59 (1999) R4741–R4744.
[58] R.D. Groot, P.B. Warren, Dissipative particle dynamics: bridging the gap between atomistic and mesoscopic simulation, J. Chem. Phys. 107 (1997) 4423–4435.
[59] P. Espanol, P. Warren, Statistical mechanics of dissipative particle dynamics, Europhys. Lett. 30 (1995) 191–196.
[60] P. Cicuta, S.L. Keller, S.L. Veatch, Diffusion of liquid domains in lipid bilayer membranes, J. Phys. Chem. B 111 (2007) 3328–3331.
[61] D. Saeki, T. Hamada, K. Yoshikawa, Domain-growth kinetics in a cell-sized liposome, J. Phys. Soc. Jpn. 75 (2006) 013602.
[62] M. Yanagisawa, M. Imai, T. Masui, S. Komura, T. Ohta, Growth dynamics of domains in ternary fluid vesicles, Biophys. J. 92 (2007) 115–125.
[63] M. Laradji, P.B.S. Kumar, Dynamics of domain growth in self-assembled fluid vesicles, Phys. Rev. Lett. 93 (2001) 198105.
[64] M. Laradji, P.B.S. Kumar, Domain growth, budding and fission in phase-separating self-assembled fluid bilayers, J. Chem. Phys. 123 (2005) 224902.
[65] S. Ramachandran, M. Laradji, P.B.S. Kumar, Lateral organization of lipids in multi-component liposomes, J. Phys. Soc. Jpn. 78 (2009) 041006.
[66] M. Laradji, P.B.S. Kumar, Anomalously slow domain growth in fluid membranes with asymmetric transbilayer lipid distribution, Phys. Rev. E 73 (2006) 040901(R).
[67] B.A. Camley, F.L.H. Brown, Dynamic simulations of multicomponent lipid membranes over long length and time scales, Phys. Rev. Lett. 105 (2010) 148102.
[68] B.A. Camley, F.L.H. Brown, Dynamic scaling in phase separation kinetics for quasi-two-dimensional membranes, J. Chem. Phys. 135 (2011) 225106.
[69] J. Fan, T. Han, M. Haataja, Hydrodynamic effects on spinodal decomposition kinetics in planar lipid bilayer membranes, J. Chem. Phys. 133 (2010) 235101.
[70] A.J. Wagner, J.M. Yeomans, Breakdown of scale invariance in the coarsening of phase-separating binary fluids, Phys. Rev. Lett. 80 (1998) 1429.

[71] A.J. Wagner, M.E. Cates, Phase ordering of two-dimensional symmetric binary fluids: a droplet scaling state, Europhys. Lett. 56 (2001) 556.
[72] M.S. Turner, P. Sens, N.D. Socci, Nonequilibrium raftlike membrane domains under continuous recycling, Phys. Rev. Lett. 95 (2005) 168301.
[73] L. Foret, Aggregation on a membrane of particles undergoing active exchange with a reservoir, Eur. Phys. J. E 35 (2012) 12.
[74] L. Foret, A simple mechanism of raft formation in two-component fluid membranes, Europhys. Lett. 71 (2005) 508.
[75] I.W. Hamley, The Physics of Block Copolymers, Oxford University Press, Oxford, 1998.
[76] J. Gómez, F. Sagués, R. Reigada, Actively maintained lipid nanodomains in biomembranes, Phys. Rev. E 77 (2008) 021907.
[77] J. Gómez, F. Sagués, R. Reigada, Nonequilibrium patterns in phase-separating ternary membranes, Phys. Rev. E 80 (2009) 011920.
[78] J. Fan, M. Sammalkorpi, M. Haataja, Domain formation in the plasma membrane: roles of nonequilibrium lipid transport and membrane proteins, Phys. Rev. Lett. 100 (2008) 178102.
[79] J. Fan, M. Sammalkorpi, M. Haataja, Lipid microdomains: structural correlations, fluctuations, and formation mechanisms, Phys. Rev. Lett. 104 (2010) 118101.
[80] J. Fan, M. Sammalkorpi, M. Haataja, Influence of nonequilibrium lipid transport, membrane compartmentalization, and membrane proteins on the lateral organization of the plasma membrane, Phys. Rev. E 81 (2010) 011908.
[81] P. Sens, M.S. Turner, Microphase separation in nonequilibrium biomembranes, Phys. Rev. Lett. 106 (2011) 238101.
[82] A.J. Levine, F.C. MacKintosh, Dynamics of viscoelastic membranes, Phys. Rev. E 66 (2002) 061606.
[83] S. Sankararaman, G.I. Menon, P.B.S. Kumar, Two-component fluid membranes near repulsive walls: linearized hydrodynamics of equilibrium and nonequilibrium states, Phys. Rev. E 66 (2002) 031914.
[84] N. Gov, A.G. Zilman, S. Safran, Hydrodynamics of confined geometries, Phys. Rev. E 70 (2004) 011104.
[85] M.L. Henle, R. McGotry, A.B. Schofield, A.D. Dinsmore, A.J. Levine, The effect of curvature and topology on membrane hydrodynamics, Europhys. Lett. 84 (2008) 48001.
[86] M.L. Henle, A.J. Levine, Hydrodynamics in curved membranes: the effect of geometry on particulate mobility, Phys. Rev. E 81 (2010) 011905.
[87] B.A. Camley, F.L.H. Brwon, Beyond the creeping viscous flow limit for lipid bilayer membranes: theory of single-particle microrheology, domain flicker spectroscopy, and long-time tails, Phys. Rev. E 84 (2011) 021904.
[88] T. Han, M. Haataja, Comprehensive analysis of compositional interface fluctuations in planar lipid bilayer membranes, Phys. Rev. E 84 (2011) 051903.
[89] C.W. Harland, M.J. Bradley, R. Parthasarathy, Phospholipid bilayers are viscoelastic, Proc. Natl. Acad. Sci. U.S.A. 107 (2010) 19146 108 (2011) 14705.
[90] S.Q. Choi, S. Steltenkamp, J.A. Zasadzinski, T.M. Squires, Active microrheology and simultaneous visualization of sheared phospholipid monolayers, Nat. Commun. 2 (2011) 312.
[91] R. Granek, Membrane surrounded by viscoelastic continuous media: anomalous diffusion and linear response to force, Soft Matter 7 (2011) 5281.
[92] S. Komura, S. Ramachandran, K. Seki, EPL 97 (2012) 68007.